

Nanoparticles Binding to Lipid Membranes: from Vesicle-Based Gels to Vesicle Tubulation and Destruction

Sarah Zuraw-Weston^{a*}, Derek A. Wood^{a*}, Ian K. Torres^a, YiWei Lee^b, Li-Sheng Wang^b, Ziwen Jiang^b, Guillermo R. Lázaro^c, ShiYu Wang^d, Avital A. Rodal^d, Michael F. Hagan^c, Vincent M. Rotello^b, and Anthony D. Dinsmore^a

^aDepartment of Physics, University of Massachusetts Amherst; ^bDepartment of Chemistry, University of Massachusetts Amherst; ^cDepartment of Physics, Brandeis University; ^dDepartment of Biology, Brandeis University

*These authors contributed equally to this work.

Supplementary Materials

In these supplemental materials, we provide additional details about methods of experiments and simulations and additional images or observational details. The sub-sections are:

1. A schematic of the sample cells used
2. Dark-field images show nanoparticle binding
3. Images of the vesicle-gel phase show adhesion induced by nanoparticles
4. Large quantities of adhered vesicles act as a solid
5. Time-sequence of three vesicles of different size within the destruction regime.
6. Images of tubulation and destruction with anionic silica (Ludox AS-30) and DOPC + cationic DOTAP lipid
7. Images of nanoparticle clusters on the vesicle surface
8. Images showing that the pore is open
9. Confocal microscope images show invaginated tubules
10. Bright-field images of multi-lamellar vesicles
11. Simulation methods
12. Estimate of the experimental threshold composition of DOPS with Au-TTMA
13. Legend for the video

1. A schematic of the sample cells used:

The process of mixing vesicles and nanoparticles was monitored *in situ* using optical microscopy so that the early stages of adsorption could be visualized. To this end, we first added vesicles into a long, narrow perfusion chamber (CoverWell™; Grace Bio Labs, with #1½ cover glass).

See Fig. S1. We then placed the chamber on the microscope and waited a few minutes to allow the vesicles to settle onto the coverslip. We then added 5 µL of nanoparticle suspension (approx. 1 mM of nanoparticles plus approx. 178 mOsm/L of glucose + sucrose with osmolarity checked) into one end of the perfusion chamber. (In some experiments, the nanoparticles were suspended in 180 mOsm/L of glucose + sucrose; these samples were not distinguishable from the others.) Particles then diffused further into the sample. This method allowed observation of the vesicles as the nanoparticles bound. Vesicles that were farther from the point of nanoparticle addition had a lower nanoparticle concentration.

Images were acquired using a CoolSnap HQ2 camera (Roper Scientific) and a Zeiss 63× Plan Neofluar objective with 1.4 NA. Confocal images were obtained on a Marianas spinning disk confocal system (3I, Inc., Denver, CO), consisting of a Zeiss Observer Z1 microscope equipped with a Yokogawa

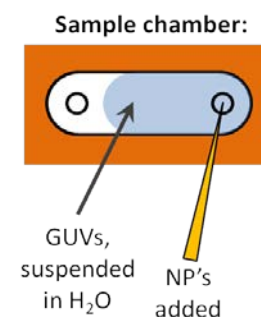


Fig. S1. Top view of perfusion chamber used for imaging the dynamics of nanoparticle/vesicle interactions.

CSU-X1 spinning disk confocal head, a QuantEM 512SC EMCCD camera, Plan Apochromat 63 \times or 100 \times oil immersion objective (1.4 NA) and Slidebook software.

2. Dark-field images show nanoparticle binding on isolated vesicles:

Dark-field optical microscopy images indicate where the nanoparticles are concentrated. The image intensity comes from light that is scattered in the sample plane and the gold particles scatter much more strongly than lipids. Fig. S2 shows example dark-field images, providing evidence that the nanoparticles have bound on a vesicle's surface.

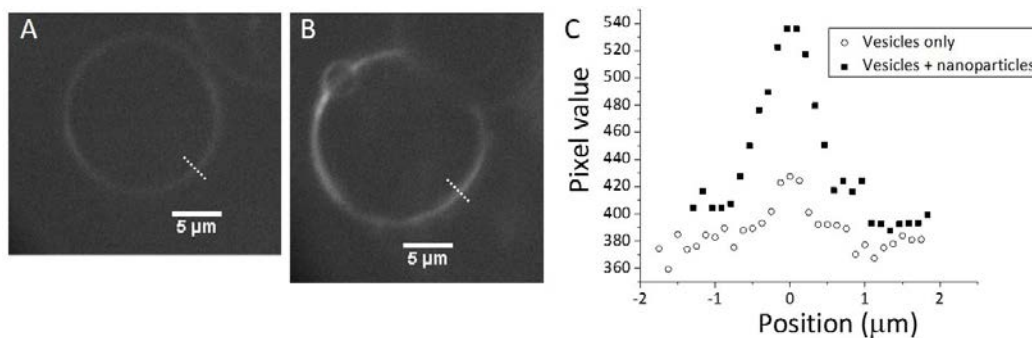


Fig. S2. (A) Dark-field image of a vesicle, showing faint contrast owing to light scattering from the membrane. (B) Dark-field image of a vesicle in the presence of nanoparticles, showing additional scattering by bound nanoparticles. (C) Plot of camera-pixel intensity *vs.* position along line segments shown by the white dashed lines in A,B. We estimated the extent of light scattering by the difference between the peak and background intensities. The values were approximately 140 and 40 with and without the particles, respectively. This approximately 3-fold enhancement of the scattering is attributed to the bound nanoparticles.

3. Images of the vesicle-gel phase show adhesion induced by nanoparticles:

Fig. S3 shows time-lapse images of vesicle adhesion on the way toward gel formation. Fig. S4 shows a dark-field image inside a vesicle gel, showing that nanoparticles accumulated at the adhesion sites.

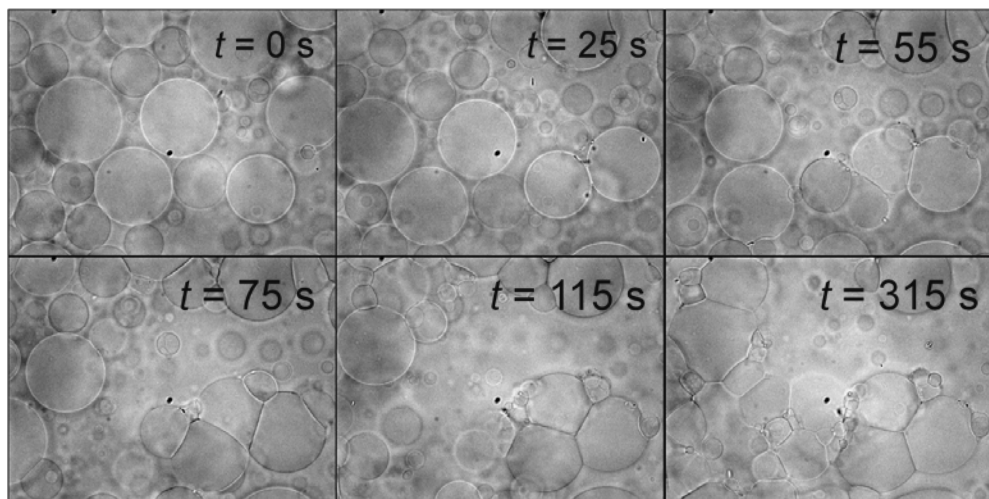


Fig. S3. Time lapse images in bright-field mode show the adhesion process of DOPC vesicles (without DOPS) as Au-TTMA nanoparticles diffused into the imaged region from the right.

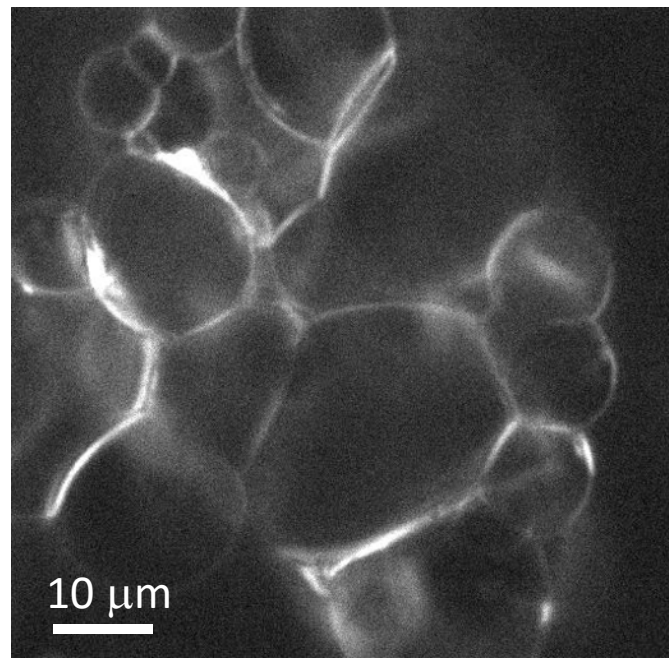


Fig. S4. Dark-field image of a vesicle gel, showing scattering from Au-TTMA nanoparticles in the adhesion regions. The membrane is composed of DOPC only.

4. Large quantities of adhered vesicles act as a solid:

To probe the mechanical properties of the vesicle-based gels, we developed an alternative system that can be made in large quantity using inexpensive, food-grade soy lecithin phosphocholine lipid (SLPC). Success in making large (50-mL) quantities shows the potential of this method for widespread application. To further expand the range of materials that can be used to form the gel, we added cationic polymer (either poly-L-lysine (150 kDa) or the more highly charged polydiallyldimethylammonium chloride (PDADMAC, 200 kDa)). With concentration 0.1% wt/vol, each polycation successfully caused aggregation of the vesicles into a gel. In all cases with polycations, we observed vesicle-vesicle adhesion and gel formation. As in the vesicle gels made with added nanoparticles (main text. Fig 1B), these vesicles remained intact as shown in Fig S5A. Even with up to 15 mol% DOPS, we never observed the destruction process, which indicates that the rigid particle shape is necessary to trigger the destruction. Figure S5B shows a 0.5 mL-sample of SLPC-vesicle gel with PDADMAC. Copper beads of diameter 270 μm were added to the suspension and were clearly supported against gravity. The support of these beads indicates that the gel material is a solid with a finite shear modulus. (In a sample of vesicles without adsorbing polymer, the copper beads settled to the bottom of the vial.) The net force on the copper beads due to gravity is on the order of μN , so that each bead applied an average pressure of roughly 10 Pa, putting a very rough lower limit on the gel's yield stress.

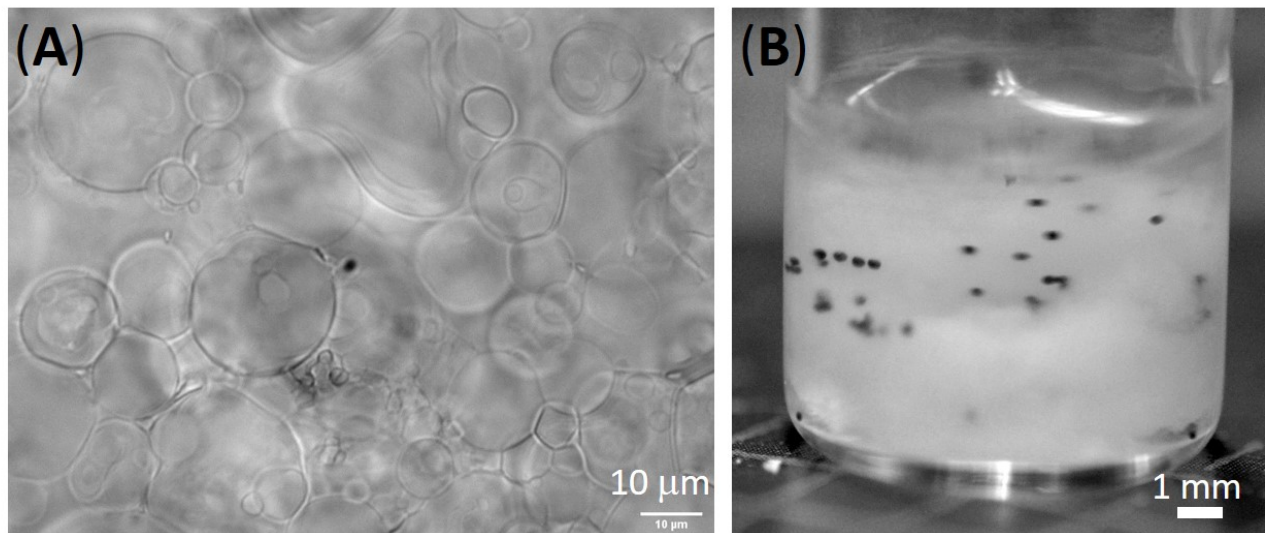


Fig. S5. Images of a gel composed of soy-lecithin PC vesicles with polycation (PDADMAC) added. (A) Optical micrograph showing that the vesicles remain intact. (B) Photograph showing that 270- μm -diameter copper beads were suspended within the gel, showing that the gel could resist shear stress and was a solid.

5. Time-sequence of three vesicles of different size within the destruction regime:

The sizes of GUVs typically ranged from a few to 30 μm in diameter. We could not discern any dependence of the behavior on the initial vesicle size. Figure S6 shows an example of three GUVs whose diameters varied by more than a factor of 2.

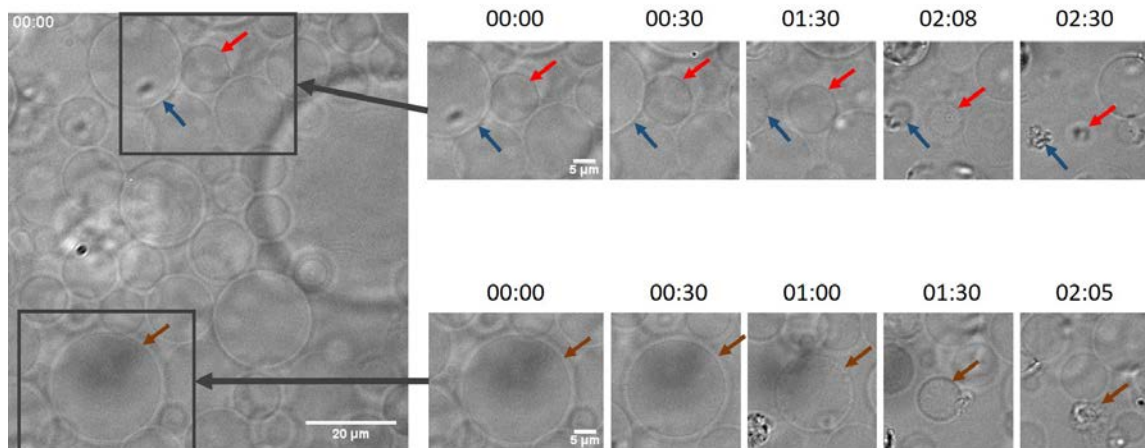


Fig. S6. Bright-field images of three different GUVs in the same field of view as they undergo destruction. The sample contains Au-TTMA particles and GUVs with 94 mol% DOPC and 6 mol% DOPS. The red, blue and brown arrows each point to a given vesicle over time. The initial vesicle diameters were 11, 21, and 25 μm , respectively. Times of each image are shown in the format, minutes:seconds.

6. Images of tubulation and destruction with anionic silica (Ludox AS-30) and DOPC + cationic DOTAP lipid:

Figure S7 shows the sequence of apparent shrinkage, pore formation, and tubulation for anionic silica (Ludox AS30) exposed to cationic-lipid-doped vesicles above threshold. The sequence of states is similar to that of Au-TTMA above threshold (*e.g.*, main text, Fig. 3).

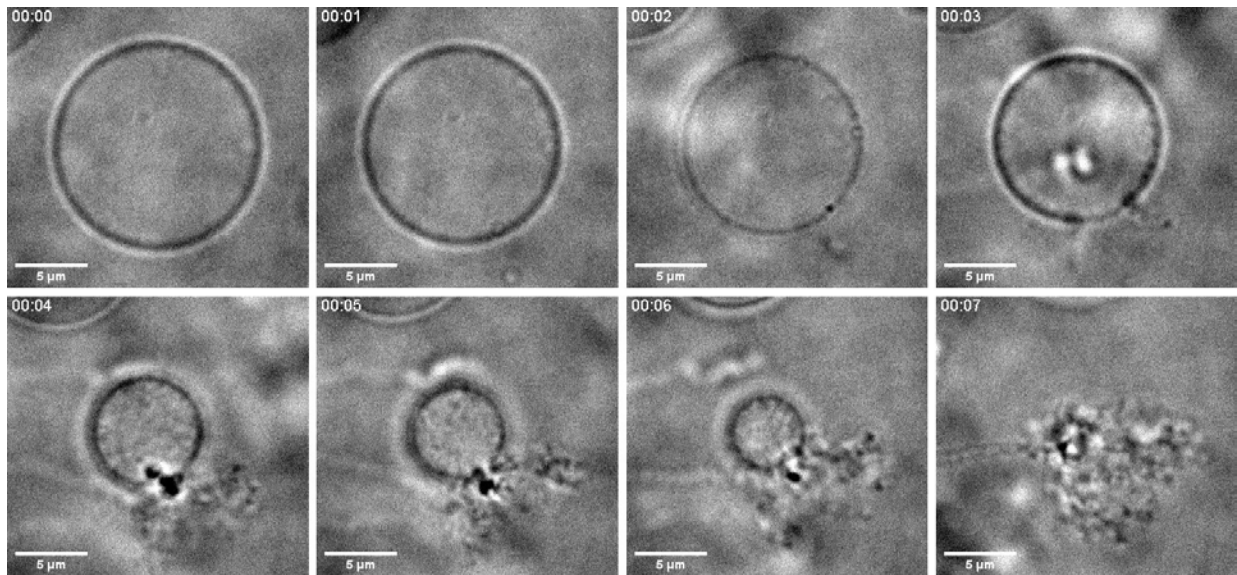


Fig. S7. A montage of brightfield micrographs showing the disruption process above threshold binding strength. This vesicle contained 29 mol% DOTAP and was exposed to silica (Ludox AS30) nanoparticles. Scale bars are all 5 μm .

7. Images of nanoparticle clusters on the vesicle surface:

Figure S8 shows two dark-field images of the Au-TTMA-nanoparticle-enriched spots that appeared on the surfaces of vesicles with DOPS concentration above threshold. These images show the same vesicle at different times and with different focal planes. Spots like this were present on every vesicle that underwent the destruction process and they remained freely diffusing throughout the process. The spots were bright under dark-field imaging, which shows that they were enriched in gold nanoparticles. These spots were always similar in size to the microscope's resolution limit, so that their true size could not be measured accurately. Figure 3C of the main text shows a similar phenomenon on bright-field, where the scattering of light by the particles made the clusters appear dark.

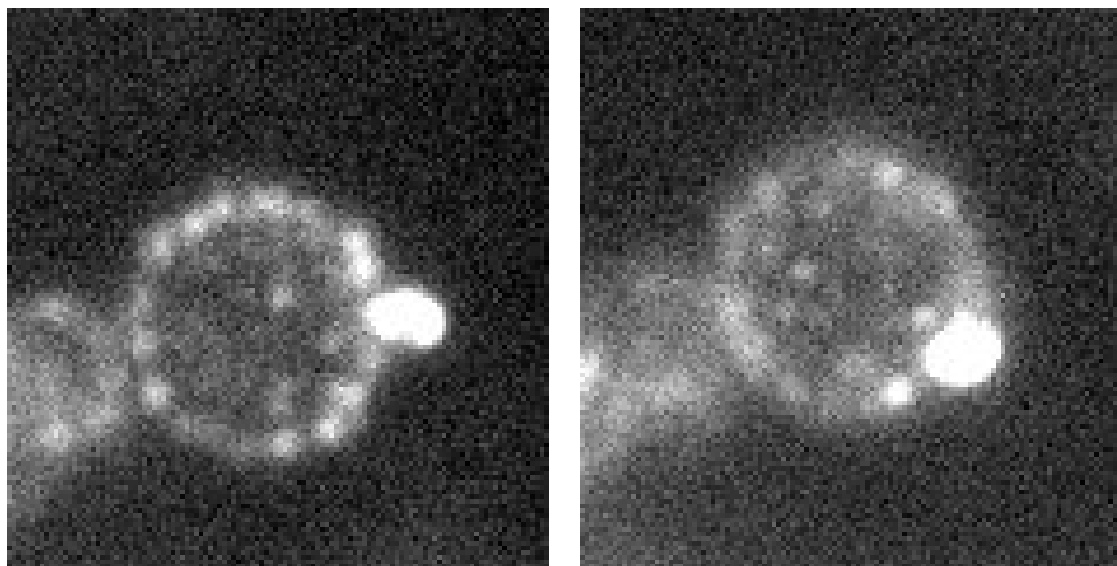


Fig. S8. Vesicles showing surface spots when the DOPS fraction exceeds the threshold value. Dark-field imaged, 4 mol% DOPS with Au-TTMA particles.

8. Images showing that the pore is open:

Figures S9 and S10 show images of two separate vesicles that contained visible contents that were expelled outward through the open pore, showing that the pores were open.

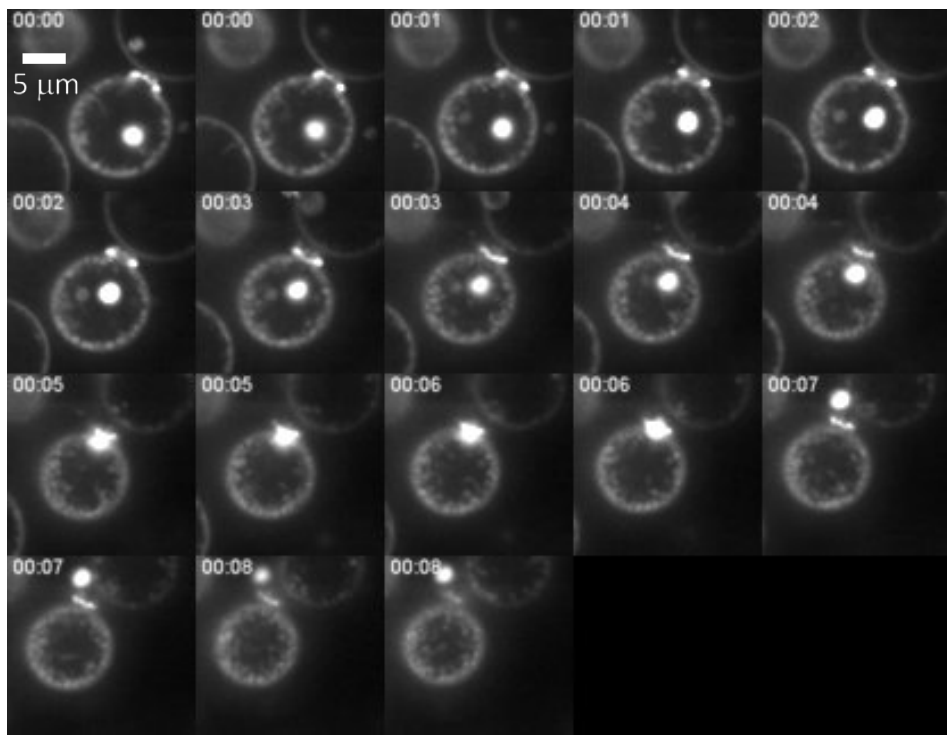


Fig. S9. A montage of images acquired with confocal fluorescence microscope. This vesicle contained 5 mol% DOPS + approximately 1 mol% Rh-DOPE and was exposed to Au-TTMA nanoparticles. Scale bar is provided in the first image. Initially, there was a large solid lipid-based object inside the vesicle. Over time, this object was forced out through the pore by the internal pressure. While this particle was inside the vesicle, it diffused slowly. It was then trapped in the pore for 3 frames, and then finally ejected a distance of more than 3 μ m in the following frame ($t = 7$ s).

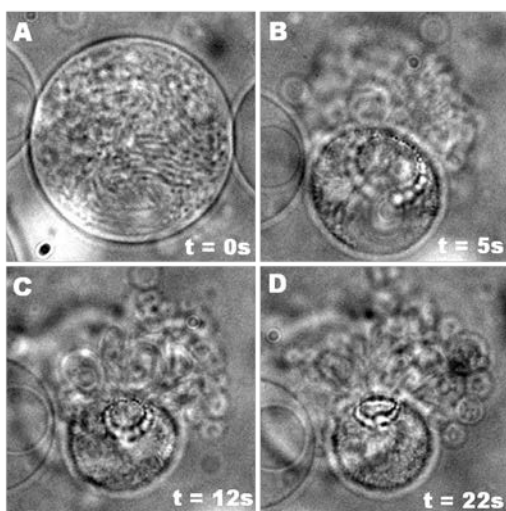


Figure S10. Bright-field microscope images show the interior contents of a vesicle with many interior compartments spilling out through a pore on the vesicle's outer surface as Au-TTMA nanoparticles bind. (5 mol% DOPS) The relative times of the images are shown in the lower-right corners. The magnification was the same in all of these images.

9. Confocal microscope images show invaginated tubules:

Figure S11 shows a confocal fluorescence image of GUVs above the crossover DOPS fraction, in the destruction regime. The lipid is fluorescent and is seen to extend into the vesicle interior in the form of a tubule.

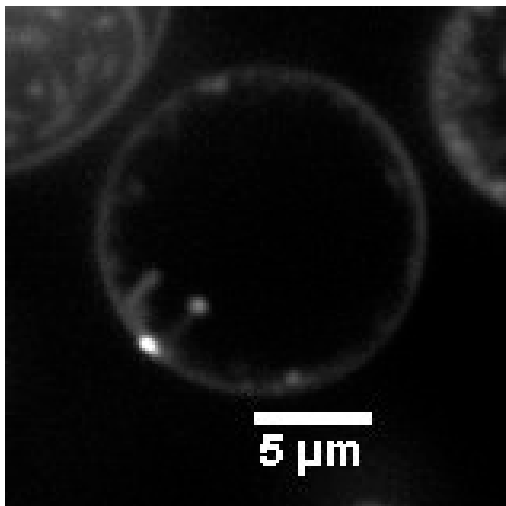


Fig. S11. A confocal microscope image of a vesicle containing 5 mol% DOPS + approximately 1 mol% Rh-DOPE, exposed to Au-TTMA nanoparticles. Inward-facing tubules (invaginations) are clearly visible in the image.

10. Bright-field images of multi-lamellar vesicles: Many vesicles in each sample contain vesicles inside them. In such cases, we observed that the outermost membrane was ‘attacked’ by the nanoparticles, as shown in Fig. S12. In such cases, the outer lamellae were peeled back and removed from the vesicle one at a time.

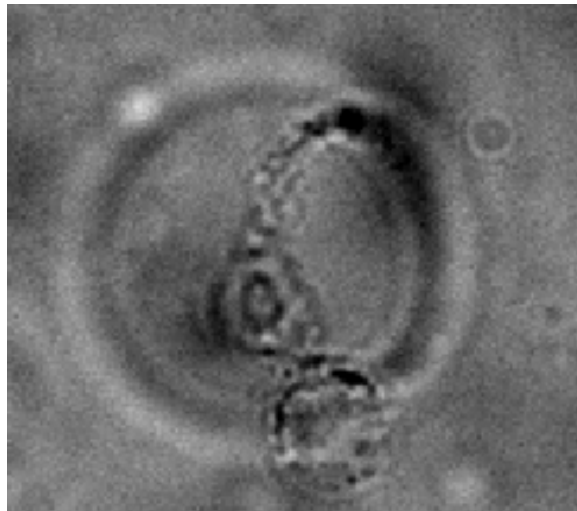


Fig. S12. Bright-field image of a multi-lamellar vesicle (5 mol% DOPS), in which the outermost lamella has been ‘attacked’ by Au-TTMA nanoparticles and peeled away.

11. Simulation methods:

Interaction potentials: Membrane model – The three pseudoatoms in each model lipid were connected through two finite extensible nonlinear elastic (FENE) bonds,

$$U_{\text{bond}}(r) = -\frac{1}{2}k_{\text{bond}}r_{\text{cut}}^2 \log[1 - (r/r_{\text{cut}})^2].$$

with maximum bond length $r_{\text{cut}} = 1.5\sigma$ and force constant $k_{\text{bond}} = 30\epsilon_0/\sigma^2$, where the reference length σ is the size of a lipid tail bead. Additionally, the first and third pseudoatoms were linked by a harmonic potential,

$$U_{\text{bend}}(r) = \frac{1}{2}k_{\text{bend}}(r - 4\sigma)^2.$$

The excluded volume of membrane beads was represented by a Weeks-Chandler-Andersen (WCA) potential¹, with the interaction between two beads with indices i and j was given by

$$U_{\text{rep}}(r) = 4\epsilon_{\text{rep}}\left[\left(\frac{b_{i,j}}{r}\right)^{12} - \left(\frac{b_{i,j}}{r}\right)^6 + \frac{1}{4}\right],$$

with $\epsilon_{\text{rep}} = 1$ and cutoff $r_{\text{cut}} = 2^{1/6}b_{i,j}$. The parameter $b_{i,j}$ depends on the types of interacting beads i and j : $b_{\text{h,h}} = b_{\text{h,t}} = 0.95\sigma$ and $b_{\text{t,t}} = 1.0\sigma$, with the subscripts ‘h’ and ‘t’ denoting head and tail beads, respectively. Hydrophobic interactions were captured by an attractive interaction between all pairs of tail beads:

$$U_{\text{hydro}}(r) = \begin{cases} -\epsilon_0, & r < r_c \\ -\epsilon_0 \cos[\pi(r - r_c)/2\omega_c], & r_c \leq r \leq r_c + \omega_c \\ 0, & r > r_c + \omega_c \end{cases}$$

with $\epsilon_0 = 1.0$ and $r_c = 2^{1/6}\sigma$. The potential width ω_c determined, among other membrane properties, the membrane bending rigidity. We set it to $\omega_c = 1.7$ so that our bending modulus was $\kappa \approx 20k_B T^2$.

Interaction potentials: Nanoparticles – We modeled nanoparticles as single beads of radius $a = 2.5$ nm. Nanoparticles interact with lipid tail beads and other nanoparticles through the repulsive component of the Lennard-Jones potential; *i.e.*, the interaction between beads i and j is

$$U_{\text{np,rep}}(r) = 4\epsilon_{\text{rep}}\left(\frac{b_{i,j}}{r}\right)^{12},$$

with $\epsilon_{\text{rep}} = k_B T$ and cutoff radius $r_{\text{off}} = b_{i,j}$. For the interaction between nanoparticles and lipid tail beads, $b_{\text{np-tail}} = 3.0$ and for the interaction between pairs of nanoparticles $b_{\text{np-np}} = 5.0$. Nanoparticles experienced an attractive interaction with lipid head beads, represented by a Lennard-Jones potential; *i.e.*, the interaction between nanoparticle i and head bead j was

$$U_{\text{np}}(r) = 4\epsilon_{\text{att}}^*\left[\left(\frac{b_{i,j}}{r}\right)^{12} - \left(\frac{b_{i,j}}{r}\right)^6\right],$$

which was cut off at $r_{\text{off}} = 6.0$ and the parameter ϵ_{att} controlled the nanoparticle-membrane attraction strength. We estimate the adhesion free energy density from the interaction potential between lipid head beads and nanoparticles following Ruiz-Herrero, *et al.*³,

$$\epsilon_a = -\gamma \log[1 + \sigma^{-1} \int_{\sigma}^{\infty} dr (e^{-U_{\text{np}}(r)} - 1)]$$

with $\gamma = 0.86/\sigma^2$ being the areal density of lipids.

Simulations – We performed simulations using HOOMD^{4,5}. We considered a tensionless membrane by simulating in the NPT ensemble, allowing box changes in the xy directions to maintain a constant membrane tension. Membrane bead positions were propagated in time using the Martina-Tobias-Klein thermostat-barostat at $k_B T = 1.1\epsilon$, $P_{xy}=0.0$, and coupling constants $\tau_T=0.5$ and $\tau_P=0.4$ for the thermostat and barostat, respectively. Nanoparticle positions were propagated using Brownian Dynamics. We performed simulations with a timestep length $\Delta t = 0.0025$, for 1.6×10^7 timesteps.

Snapshot images of tubules that formed in simulations are shown in Fig. S13. We discerned two kinds of tubules: U and I, as defined in the figure.

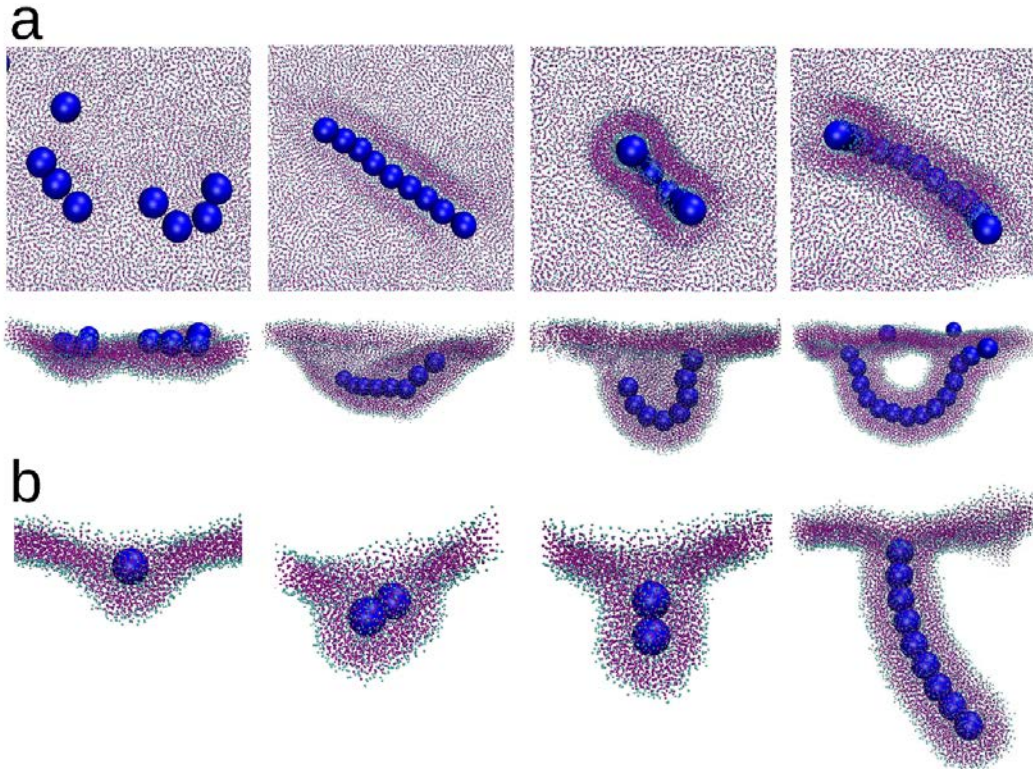


Fig. S13. Representative simulation trajectories illustrating the pathways of tubule formation. **(a)** Snapshots showing the formation of a ‘U-tubule’, meaning that the tubule is connected to the membrane at both ends. Particles initially formed a linear aggregate on the relatively flat membrane; subsequently the membrane wrapped the aggregate leading to tubulation. **(b)** Snapshots showing I-tubule formation, meaning that the tubule is connected to the membrane only at one end. Formation began with envelopment of two NPs, forming a duplet oriented normal to the membrane. The tubule then extended through diffusion and association of additional NPs.

12. Estimate of the experimental threshold composition of DOPS with Au-TTMA:

Guided by the simulations, we used the threshold criterion that $wa^2/\kappa = \frac{1}{2}$, where w is the adhesion free energy per area, a is the particle radius (3.4 nm in the Au-TTMA experiments), and κ is the membrane bending energy (8.2×10^{-20} J, appropriate for DOPC⁶). We used Poisson-Boltzmann theory to account for the electrostatic double-layer interaction between the membrane (treated as a plane) and the spherical particle. The dopant lipids were treated as a mean-field charge density, which is justified by the fact that the patch of membrane wrapping each particle had, on average, several charged lipids (*i.e.*, more than one). Assuming the lipids were uniformly distributed, the number of charged-lipid molecules per nanoparticle area, per membrane leaflet at threshold was approximately eight for the Au-TTMA system, 183 for the silica Ludox AS30, and 200 for Ludox SM.

The membrane potential can be taken as the sum of the pure-DOPC potential (-9 mV from electrophoretic mobility⁷) plus the potential coming from a charge of $-e$ per DOPS, where e is the fundamental charge, 1.6×10^{-19} C. We consider only the charge on the outer leaflet of the membrane. The Au-TTMA surface charge density can be obtained from the ligand density (77 ± 4 per particle⁸). The quaternary ammonium groups at the ligand termini have a permanent positive charge, which gives a charge

density of approximately 0.5 e/nm^2 . (Extracting charge density from the measured zeta potential of 18 mV gives a much lower density of roughly 0.02 e/nm^2 but this is not a reliable method to obtain surface charge⁹. The same caution applies to the pure DOPC membrane, but we have no other means to estimate surface charge density.) Using these estimates and applying the condition $wa^2/\kappa = 1/2$, we estimate a threshold composition as low as 3 mol% DOPS, or as high as 70 mol% DOPS for the (likely inaccurate) lower estimate of the nanoparticle charge from zeta potential.

This estimate neglects two phenomena that may be quantitatively important. First, the DOPS lipids should tend to accumulate near the nanoparticles, which increases the double-layer interaction at the cost of lowering their entropy. A prior theoretical treatment of this effect estimated that in a zwitterionic PC-lipid membrane with 10 mol% anionic lipid, in-plane rearrangements enhance the binding free energy of a cationic rod-shaped particle by a factor of approximately 1.7.¹⁰ In the present case, the effect seems to us likely to be of the same order of magnitude. Second, treating the nanoparticle-membrane interaction in terms of adhesion per area is a crude approximation because the range of interaction (set by the Debye length of 2 nm or more) is comparable to particle size.

Nonetheless, the rough estimate serves to show that a threshold composition of a few mol% DOPS is consistent with the prediction of $wa^2/\kappa = 1/2$. These estimates also guide predictions of how parameters such as charge density, salinity and membrane modulus should affect the threshold composition.

13. Legend for the video

The movie shows the time evolution of a single giant unilamellar vesicle (GUV) with 96 mol% DOPC and 4 mol% DOPS as Au-TTMA nanoparticles bind. This sample is above threshold and the process of inversion and destruction can be seen. The first image shows a 10-μm scale bar. During the video, the vesicle diffused but the microscope focus was adjusted to maintain focus approximately at the GUV's 'equator.' The image was made with an optical microscope in dark-field mode, so that the bright regions correspond to strong scattering of light, which is predominantly from nanoparticles. Near the start of the video, bright particle clusters can be seen near the top right surrounding a pore in the vesicle.

References for Supplemental Section

1. Weeks, J. D., Chandler, D. & Andersen, H. C. Role of Repulsive Forces in Determining Equilibrium Structure of Simple Liquids. *J. Chem. Phys.* **54**, 5237 (1971).
2. Cooke, I. R., Kremer, K. & Deserno, M. Tunable generic model for fluid bilayer membranes. *Physical Review E* **72** (2005).
3. Ruiz-Herrero, T., Velasco, E. & Hagan, M. F. Mechanisms of Budding of Nanoscale Particles through Lipid Bilayers. *J. Phys. Chem. B* **116**, 9595-9603 (2012).
4. Nguyen, T. D., Phillips, C. L., Anderson, J. A. & Glotzer, S. C. Rigid body constraints realized in massively-parallel molecular dynamics on graphics processing units. *Comput. Phys. Commun.* **182**, 2307-2313 (2011).
5. Anderson, J. A., Lorenz, C. D. & Travesset, A. General purpose molecular dynamics simulations fully implemented on graphics processing units. *J. Comput. Phys.* **227**, 5342-5359 (2008).
6. Nagle, J. F., Jablin, M. S., Tristram-Nagle, S. & Akabori, K. What are the true values of the bending modulus of simple lipid bilayers? *Chem. Phys. Lipids* **185**, 3-10 (2015).
7. Needham, D. & Zhelev, D. in *Perspectives in Supramolecular Chemistry: Giant Vesicles* (eds. Luisi, P. L. & Walde, P.) (John Wiley & Sons, Hoboken, NJ, 2007).
8. Jiang, Y. et al. The Interplay of Size and Surface Functionality on the Cellular Uptake of Sub-10 nm Gold Nanoparticles. *ACS Nano* **9**, 9986-9993 (2015).
9. Bhattacharjee, S. DLS and zeta potential - What they are and what they are not? *J. Control. Release* **235**, 337-351 (2016).

10. Haugen, A. & May, S. The influence of zwitterionic lipids on the electrostatic adsorption of macroions onto mixed lipid membranes. *J. Chem. Phys.* **127**, 215104 (2007).